PCCP

PAPER

View Article Online
View Journal | View Issue

Cite this: *Phys. Chem. Chem. Phys.*, 2014, **16**, 15917

Adsorption and photocatalytic splitting of water on graphitic carbon nitride: a combined first principles and semiempirical study

Jonas Wirth,*[a] Rainer Neumann,[a] Markus Antonietti[b] and Peter Saalfrank[a]

Received 9th May 2014,
Accepted 19th June 2014

DOI: 10.1039/c4cp02021a

www.rsc.org/pccp

Graphitic carbon nitride, g-C_3N_4, is a promising organic photo-catalyst for a variety of redox reactions. In order to improve its efficiency in a systematic manner, however, a fundamental understanding of the microscopic interaction between catalyst, reactants and products is crucial. Here we present a systematic study of water adsorption on g-C_3N_4 by means of density functional theory and the density functional based tight-binding method as a prerequisite for understanding photocatalytic water splitting. We then analyze this prototypical redox reaction on the basis of a thermodynamic model providing an estimate of the overpotential for both water oxidation and H^+ reduction. While the latter is found to occur readily upon irradiation with visible light, we derive a prohibitive overpotential of 1.56 eV for the water oxidation half reaction, comparing well with the experimental finding that in contrast to H_2 production O_2 evolution is only possible in the presence of oxidation cocatalysts.

1 Introduction

In recent years graphitic carbon nitride of the approximate composition C_3N_4 has attracted broad attention due to its promising electronic properties.[1,2] Being an electron rich organic semiconductor with an experimental band gap of 2.7 eV, graphitic carbon nitride (g-C_3N_4) has been found to drive a variety of photo-catalytic redox reactions such as water[3,4] and CO_2 (ref. 5) reduction, alcohol oxidation and oxidative dehydrogenation of amines.[6] At the same time the material is relatively easy to prepare, inexpensive and of high mechanical, thermal and chemical stability,[1] rendering g-C_3N_4 a promising catalyst for large-scale applications.

In this context one major advantage of graphitic carbon nitride as compared to conventional catalysts is being metal-free and therefore tolerating chemical functionality in reactant molecules.[2] Still, the catalytic rates for most reactions are rather low if pure g-C_3N_4 is used. It can be increased by adding cocatalysts such as platinum for water reduction[4] which sacrifices, however, some of the material's before-mentioned advantages. In a different approach the material itself was modified, *e.g.* by doping with heteroatoms such as fluorine or sulfur or *via* copolymerization with barbituric acid, significantly raising H_2 production rates (see ref. 1, 7 and references therein). To further improve the material properties in a systematic manner, however, a microscopic understanding of g-C_3N_4 photocatalysis is crucial.

Being of potential technological interest in the context of "green" energy conversion and storage and at the same time being "simple" enough, the photocatalytic water splitting reaction is a natural starting point for a theoretical approach to photocatalysis on graphitic carbon nitride. As estimated from photoelectrochemical studies and density functional theory (DFT) band structure calculations for g-C_3N_4,[1,8] its valence and conduction bands seem to perfectly engulf the redox potentials of both water splitting half reactions according to eqn (1) and (2) (see Fig. 1). Therefore, in principle and purely following these energetic arguments, graphitic carbon nitride should be able to catalyze both H_2O oxidation and H^+ reduction independently and without any help of additional reagents:

$$2H_2O \rightarrow O_2 + 4H^+ + 4e^- \quad (1)$$

$$4H^+ + 4e^- \rightarrow 2H_2 \quad (2)$$

In practice, however, a sacrificial electron donor (*e.g.* triethanolamine) is needed for H_2 production and an electron acceptor such as $AgNO_3$ for water oxidation, respectively,[3,4] to avoid recombination of intermediates (otherwise spatial separation of anodic and cathodic reaction would be required). Additionally, both half reactions are subject to an intrinsic overpotential increasing the effective (photo-generated) potential bias needed for the individual half reaction to take place. In fact, the water oxidation reaction seems to suffer from a very high overpotential

[a] *University of Potsdam, Institute of Chemistry, Karl-Liebknecht-Straße 24-25, 14476 Potsdam, Germany. E-mail: jowirth@uni-potsdam.de*
[b] *Max-Planck Institute of Colloids and Interfaces, Research Campus Golm, Am Mühlenberg 1, 14476 Potsdam, Germany*

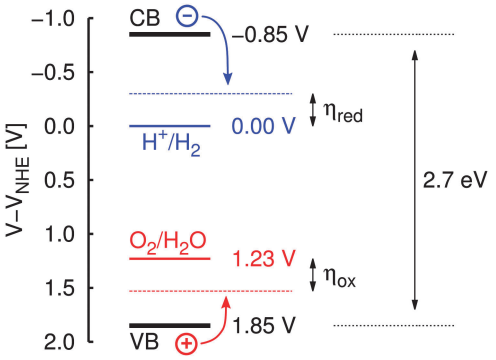

Fig. 1 Schematic illustration of band positions in g-C_3N_4 (at pH = 7) relative to the normal hydrogen electrode (NHE) as given in ref. 8. VB/CB: valence/conduction band; η_{ox}/η_{red}: overpotential for water oxidation/H^+ reduction.

preventing the reaction to proceed without help of additional cocatalysts.[3,4]

Accordingly, two major steps towards a microscopic picture of g-C_3N_4 photocatalysis are:

1. Understanding the microscopic interaction between catalyst, reactants and products which contribute to observable overpotentials.

2. Understanding charge separation, localization and exciton lifetime in graphitic carbon nitride.

The focus of this article is on the first point, especially on the question of water adsorption as a prerequisite for photocatalytical water oxidation. Different graphitic carbon nitride surfaces were studied systematically in terms of the adsorption of water molecules on variable surface terminations. Subsequently, a four-step mechanism for the photocatalytic water oxidation reaction, previously applied to transition metal oxide surfaces, was adopted and the corresponding overpotential was derived by means of first principles thermodynamics; for comparison, a similar approach was set up for H^+ reduction, as well.

The article is organized as follows: After this introduction the applied methodology will be explained, followed by a detailed account on the studied model systems (Section 2). In Section 3 first the water adsorption on two different surface terminations will be discussed, subsequently the overpotentials for the two water decomposition half reactions on a carbon nitride substrate will be derived using a thermodynamic model. Finally, the findings of this account will be summarized and further steps towards a detailed understanding of g-C_3N_4 photocatalysis will be proposed.

2 Models and methods

2.1 Computational details

To allow for the study of different structural patterns including not only two-dimensional but also multilayer periodic models, a combined first-principles and semiempirical approach was chosen. Gradient-corrected density functional theory (DFT) was used for the purpose of benchmarking and for obtaining quantitative results, complemented by density functional based tight-binding (DFTB) calculations for gaining more qualitative information on the basis of extended models and otherwise inaccessible geometries.

Periodic first-principles total energy calculations were performed within the framework of Kohn–Sham DFT[9] using the projector augmented wave (PAW) approach[10,11] as implemented in the Vienna ab initio simulation package (VASP).[12–14] Electron exchange and correlation were treated within the generalized gradient approximation (GGA) using the PBE functional.[15,16] Total energies were corrected for dispersion interaction by applying Grimme's semiempirical D3 scheme[17] with the damping function for short interatomic distances according to Becke and Johnson (see ref. 18 and references therein). In case of radical species involved in the model description of water decomposition on the substrate, spin-polarized calculations were performed.

After systematic convergence studies, total and adsorption energies were found to be sufficiently accurate using a plane-wave basis set truncated at an energy cutoff of 400 eV and a Γ-point centered ($3 \times 3 \times 1$) Monkhorst–Pack grid[19] (resulting in a set of 5 irreducible k-points) for sampling the Brillouin zone of the hexagonal supercell. Self-consistent field convergence was considered sufficient for a total energy difference of less than 10^{-4} eV between iterations; ionic relaxation was stopped when the forces acting on ions dropped below 0.01 eV $Å^{-1}$.

To treat larger systems, semiempirical DFTB calculations were performed using the DFTB + package.[20] A self-consistent charge (SCC) approach was chosen to account for possible asymmetric charge distributions using the B3LYP/6-31G* parametrization according to Elstner and coworkers;[21] dispersion forces were included by introducing pair-wise interatomic potentials of the Lennard-Jones type with parameters taken from the Universal Force Field (UFF)[22] and a damping scheme for short interatomic distances.[23] To sustain consistency with first-principles calculations in case of periodic calculations, the Brillouin zone of the hexagonal supercell was also sampled using a Γ-point centered ($3 \times 3 \times 1$) Monkhorst–Pack grid. SCC convergence was found to be ensured for a limit of 10^{-5} e difference for any charge between two consecutive cycles; ionic relaxation was stopped when every individual force component dropped below 0.005 eV $Å^{-1}$.

Both in DFT and SCC-DFTB optimizations all atoms were free to move unless stated otherwise. This also applies for normal mode analysis, *i.e.* diagonalization of the dynamical (Hessian) matrix; energy derivatives with respect to the nuclear coordinates were evaluated numerically using centered finite differences. To reduce the computational effort, vibrations were obtained at the Γ-point only. This approximation is justified by the large unit cell on the one hand, on the other hand enthalpy contributions due to phonon dispersion will cancel out by a large extent, since we are mainly interested in free energy differences.

2.2 Thermodynamics and photoelectrochemistry

The adsorption energy for any adsorbate species A was evaluated as the energy difference

$$\Delta E_{ads} = E_{*A} - (E_* + E_A), \quad (3)$$

with * denoting the bare surface and *A indicating adsorption of species A on the surface. To ensure error cancellation, equal computational settings were applied to all species involved.

Free energies $G(T) = E + H(T) - TS(T)$, with E denoting the self-consistent field energy for a given species, were calculated including all relevant finite temperature contributions to enthalpy $H(T)$ and entropy $S(T)$, *i.e.* vibration, rotation and translation for gas phase species; for adsorbed species only vibrational contributions were considered since rotational and translational motions become frustrated. The individual contributions were calculated following standard procedures as outlined in ref. 24.

The water-splitting reaction was modelled according to an approach originally used by Nørskov and coworkers to clarify the origin of the overpotential for oxygen reduction on a platinum (111) surface.[25] The method was later also applied to water oxidation on different metal oxide surfaces.[26–28] In this approach the overall anodic reaction according to eqn (1) is decomposed into four one-electron steps A–D, each one providing a proton and an electron:

$$\text{A:} \quad * + H_2O \rightarrow *OH + H^+ + e^-, \quad (4)$$

$$\text{B:} \quad *OH \rightarrow *O + H^+ + e^-, \quad (5)$$

$$\text{C:} \quad *O + H_2O \rightarrow *OOH + H^+ + e^-, \quad (6)$$

$$\text{D:} \quad *OOH \rightarrow * + O_2 + H^+ + e^-. \quad (7)$$

For each reaction step the free energy difference under influence of finite pH and a potential bias U can be written as follows:[26–28]

$$\Delta G_A = G_{*OH} + \tfrac{1}{2}G_{H_2} - G_{H_2O} - G_* - \Delta_{pH} - eU, \quad (8)$$

$$\Delta G_B = G_{*O} + \tfrac{1}{2}G_{H_2} - G_{*OH} - \Delta_{pH} - eU, \quad (9)$$

$$\Delta G_C = G_{*OOH} + \tfrac{1}{2}G_{H_2} - G_{H_2O} - G_{*O} - \Delta_{pH} - eU, \quad (10)$$

$$\Delta G_D = G_* + \tfrac{1}{2}G_{H_2} - G_{O_2} - G_{*OOH} - \Delta_{pH} - eU. \quad (11)$$

Here, the free energy of H^+ and e^- has been replaced by $\frac{1}{2}G_{H_2}$ considering the reaction $\frac{1}{2}H_2 \rightarrow H^+ + e^-$ at standard conditions of pressure and temperature. Furthermore, an overall shift of the free energy is imposed on every reaction step to include both the pH dependence of the redox potential ($\Delta_{pH} = k_B T \ln(10) \cdot pH$) as well as a potential bias due to a light-induced exciton and/or external potential ($-eU$). All thermochemistry data was obtained for T = 300 K; the translational finite-temperature contribution to the free energy of H_2O was calculated at the equilibrium pressure of 0.035 bar to simulate liquid water, whereas G_{O_2} and G_{H_2} were calculated at 1 bar. Note, that (in contrast to ref. 27 for example) the free energy difference for the water decomposition reaction $H_2O \rightarrow 0.5O_2 + H_2$ was not fixed at the experimental value here; thus, only DFT-derived free energies enter the equations and support a consistent description of thermodynamics.

Similarly, the cathodic H^+ reduction half reaction can be decomposed into two one-electron steps E and F, each consuming a proton and an electron:

$$\text{E:} \quad * + H^+ + e^- \rightarrow *H, \quad (12)$$

$$\text{F:} \quad *H + H^+ + e^- \rightarrow * + H_2. \quad (13)$$

Or, assuming the involvement of another water molecule:

$$\text{E}': \quad *H_2O + H^+ + e^- \rightarrow *H_3O, \quad (14)$$

$$\text{F}': \quad *H_3O + H^+ + e^- \rightarrow *H_2O + H_2. \quad (15)$$

Accordingly, the free energy difference under influence of finite pH and a potential bias U can be written as

$$\Delta G_E = G_{*H} - G_* - \tfrac{1}{2}G_{H_2} - \Delta_{pH} - eU, \quad (16)$$

$$\Delta G_F = G_* + G_{H_2} - G_{*H} - \tfrac{1}{2}G_{H_2} - \Delta_{pH} - eU, \quad (17)$$

and

$$\Delta G_{E'} = G_{*H_3O} - G_{*H_2O} - \tfrac{1}{2}G_{H_2} - \Delta_{pH} - eU, \quad (18)$$

$$\Delta G_{F'} = G_{*H_2O} + G_{H_2} - G_{*H_3O} - \tfrac{1}{2}G_{H_2} - \Delta_{pH} - eU, \quad (19)$$

respectively.

It should be noted that in this approach no explicit photoexcitation is described but the effect of photo-generated electrons is included *via* the shift of the individual reaction free energies by $-eU$. In ref. 27 the notion that the difference between the potential of a hole in the valence band of the catalytic substrate and the redox potential for O_2 evolution is basically the driving force for photocatalytic water oxidation was used to decide whether or not the reaction will proceed spontaneously upon irradiation of the sample. This can be done by testing if each step in the free energy profile according to eqn (8) to (11) is downhill under the influence of the potential of a hole in the substrate valence band or, alternatively, by comparing the free energy of this hole with the reaction free energy of the water splitting reaction plus its associated overpotential. The latter is given by the difference between the potential needed for the overall reaction to be energetically neutral and the one causing every individual reaction step to be downhill in energy.

2.3 Structural models

Different g-C_3N_4 structural models with increasing complexity were set up for this study. All of them are based on the tri-*s*-triazine **4** building block that is believed to form from melamine **3** at around 390 °C in the thermal synthesis of graphitic carbon nitride starting from cyanamide **1** or dicyandiamide **2** (see ref. 2 and Fig. 2). The resulting tri-*s*-triazine based pattern **5** was shown to be thermodynamically more favourable than other possible triazine based g-C_3N_4 allotropes, both by plane-wave DFT within the local density[29] and generalized gradient approximations,[30] as well as by using a localized Gaussian-type basis in combination with the B3LYP hybrid functional.[31] Furthermore, tri-*s*-triazine based g-C_3N_4 sheets

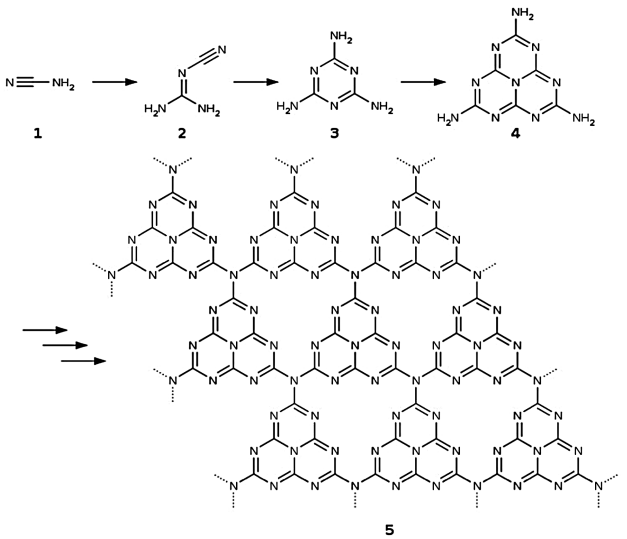

Fig. 2 Schematic representation of the reaction sequence starting from cyanamide **1** and leading *via* dicyandiamide **2**, melamine **3** and tri-*s*-triazine **4** to the formation of graphitic carbon nitride **5** in its thermodynamically most stable form (according to ref. 2).

were found to be subject to strong lateral reconstruction, resulting in a wave-like pattern of the individual units.[30,31]

2.3.1 Periodic one-layer model based on DFT. To include this feature as well as its structural and electronic implications for water adsorption and electrochemical splitting, a (3 × 3) supercell according to Fig. 3 was selected as a model for an extended g-C_3N_4 sheet and used throughout all first-principles calculations. Since graphitic carbon nitride was found to be rather stable with respect to oxidation (photoelectrochemical cells can even be run under oxygen atmosphere[8]), no higher oxidation states are considered for the substrate at this point. The lattice parameters were optimized as $a = b = 20.37$ Å,

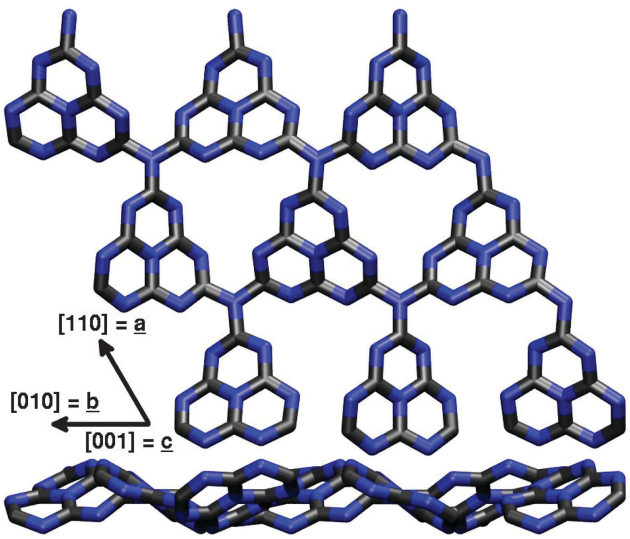

Fig. 3 Top and side view of the (3 × 3) supercell model for an extended g-C_3N_4 sheet corresponding to the (0001) surface of a layered graphite-like bulk structure used in the first principles calculations. Carbon atoms are displayed in black, nitrogen atoms in blue color, respectively.

corresponding to a compression of the lattice by 0.34 Å per tri-*s*-triazine unit with respect to the non-reconstructed (plane) surface. Taking the in-plane distance between two nitrogen atoms in the center of neighbouring tri-*s*-triazine units (which is largely consistent in the buckled supercell) as a measure for the lateral periodicity of the material, we arrive at 6.79 Å for the PBE-based first-principles calculations. This is in very good agreement with previously published 6.77 Å derived from GGA *ab initio* molecular dynamics (AIMD) simulations,[30] as well as with experimentally observed 6.81 Å from X-ray powder diffraction (XRD) patterns.[3] All of this suggests that the wave-like sheet structure of g-C_3N_4 is properly reproduced in the applied model. A calculated band gap of 2.19 eV also compares reasonably well, considering the GGA-typical underestimation of this quantity,[32] with the optical band gap of 2.7 eV found by UV-Vis spectroscopy.[3]

2.3.2 Periodic multi-layer models based on SCC-DFTB. Nevertheless, the transferability of this single-layer approach to larger and higher-dimensional structures which are definitely present in experiment was additionally tested by means of computationally less demanding SCC-DFTB calculations. Therefore, in a first step the lateral reconstruction for a single g-C_3N_4 layer was studied by systematically increasing the supercell size in periodic SCC-DFTB calculations while at the same time optimizing cell parameters as well as internal atomic positions. Apart from the previously observed (3 × 3) reconstruction, however, no further effect was found up to a supercell size of (6 × 6) tri-*s*-triazine units, rendering the chosen cell size perfectly suitable to capture the lateral structural periodicity. Interestingly, however, the SCC-DFTB optimized lattice parameter for the reconstructed cell was found to be 7.00 Å per tri-*s*-triazine unit, corresponding to a less pronounced buckling of the g-C_3N_4 sheet. Although this is not perfectly consistent with the DFT calculations, it compares very well with the B3LYP-based value of 7.11 Å published by Deifallah and coworkers.[31] Obviously, the difference in buckling behaviour follows methodic lines; whether, however, the effect is due to the added exact exchange in the B3LYP approach, the differences in the functional, or the rather small basis sets applied (6-21G* in case of ref. 31) cannot be said at this point.

In a second step, following previous work of Gracia and Kroll,[30] we also studied the effect of additional g-C_3N_4 layers stacked in a graphite-like manner by means of SCC-DFTB calculations. Consistently, an ABAB stacking pattern of corrugated g-C_3N_4 layers was found to be the most stable conformation, placing holes and tri-*s*-triazine units of consecutive layers on top of each other (*cf.* Fig. 4). The lattice parameters of the corresponding bulk structure with a unit cell of two (3 × 3) layers were optimized as $a = b = 20.98$ Å and $c = 6.65$ Å, showing hardly any stacking effect on the lateral cell size as compared to the single-layer optimization; the corresponding interlayer distance of 3.33 Å compares almost perfectly with the experimental value of 3.26 Å derived from wide-angle X-ray scattering (WAXS) measurements.[2] Concerning the electronic band gap of the system, a value of 2.80 eV was found for the single-layer model using DFTB, comparing very well with the experimental 2.7 eV; this almost perfect agreement, however, is rather likely to result from error compensation, given the much higher 3.82 eV found in a

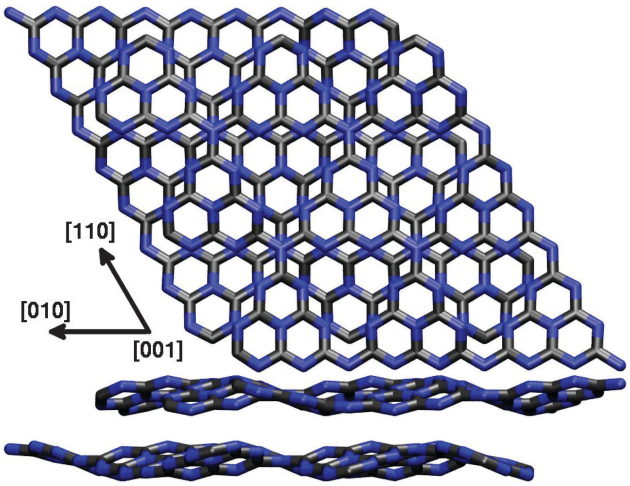

Fig. 4 Top and side view of the SCC-DFTB optimized (3 × 3) bulk unit cell for an ABAB g-C_3N_4 crystal.

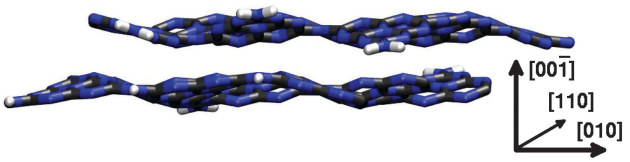

Fig. 5 Top view of the ($\bar{1}$010) surface of an ABAB g-C_3N_4 crystal, featuring residual hydrogen atoms along the cutting edge (displayed in white).

corresponding B3LYP study.[31] Just as the lattice parameters, also the band gap was found to be largely independent from additional layers (2.85 eV for the bulk model), supporting the idea that a single-layer description of the surface is sufficient for the problems at hand. This, however, we can only tell from the point of view provided by the applied methodology, which includes only empirical dispersion corrections to the total energy and is not able to capture possible effects due to *explicit* electron–electron interaction. The influence of additional layers on the (0001) surface and its adsorption properties will be discussed in Section 3.1.

Introducing the third dimension most naturally raises the question of different crystal surfaces that might play a role in experiment. Especially the six identical surfaces of the ($\bar{1}$010) type that can be created by clean cuts along a row of tri-*s*-triazine units in the direction of in-plane lattice vector ***a*** or ***b*** might exhibit different properties due to residual hydrogen atoms from synthesis (*cf.* Fig. 2) which saturate the bridging nitrogens between neighbouring tri-*s*-triazine units. Since the corresponding unit cell (see Fig. 5) needs to consist of at least two g-C_3N_4 layers, this structure was studied using the computationally less demanding SCC-DFTB approach only.

3 Results and discussion

3.1 Water adsorption

3.1.1 The (0001) surface. Beginning our study of water adsorption, we focus on the (0001) surface of a perfect g-C_3N_4 ABAB crystal (*cf.* Fig. 4). Since it was shown by means of SCC-DFTB that additional layers do not trigger any observable change in the lattice constants of the material (see Section 2.3), in a first step we studied the adsorption properties of the (0001) surface by periodic DFT calculations based on a single layer model (Fig. 3). In order to have a solid basis not only for further studies concerning photocatalytic water splitting or H^+ reduction but also for benchmarking our supporting semiempirical calculations, a rather broad approach was chosen by performing a relaxed potential energy surface (PES) scan for the adsorption of a single water molecule per (3 × 3) supercell. Fortunately, considering the symmetry of the reconstructed surface with its tilted tri-*s*-triazine units each of which providing a very similar, albeit rotated, chemical environment, the scan could be reduced to a single unit plus its neighbouring hole, corresponding to one former unit cell of the unreconstructed structure (see Fig. 6(a)). The selected surface area was scanned on a 10 × 10 grid by freezing the lateral coordinates of the water oxygen atoms while relaxing all remaining, including the surface's, degrees of freedom. Also, for each grid point different starting orientations of the water hydrogen atoms relative to the surface were tested to arrive at reliable data.

The resulting PES is presented in Fig. 6(b). The two lateral coordinates are given in units of fractions x_a and x_b of the length of the full lattice vectors ***a*** and ***b***. First of all we find one distinct minimum around x_a = 0.33 and x_b = 0.51 above the triangular hole in the slab (the apparent minimum at large x_a and x_b is in fact the same but in the next subcell). This minimum is more stable by approximately 0.37 eV with respect to the least favourable water position on top of the tri-*s*-triazine unit at x_a = 0.51 and x_b = 0.42. The reason for this stabilization becomes clear from the fully optimized adsorption geometry shown in Fig. 7, allowing for hydrogen bonding interaction between the water H atoms and the electron lone pairs at the N atoms of opposing tri-*s*-triazine units. The tilted orientation of the water molecule with respect to the surface normal maximizes electrostatic interaction between the negatively polarized water oxygen ($-1.3e$) and the closest, positively polarized carbon atom ($+1.5e$) in the tri-*s*-triazine unit as estimated from Bader charge analysis[33] (note, however, that this is a purely qualitative measure for the charge distribution inside the system). The adsorption energy according to eqn (3) for this configuration is E_{ads} = −0.62 eV, corresponding to strong physisorption. For comparison and to rule out possible overbinding of the PBE-D3 scheme, the adsorption energy was also calculated using the non-local van-der-Waals density functional of Dion and coworkers,[34–36] including re-optimization of the structures obtained in the PBE-D3 approach but retaining the preassigned lattice constants as well as all computational settings. The resulting water adsorption geometry, however, hardly changes with respect to the PBE-D3 case and gives rise to a marginally shifted adsorption energy of −0.55 eV, confirming our original computational protocol.

To the authors' knowledge there is only one previous publication about water adsorption on graphitic carbon nitride to compare with.[37] This periodic first-principles (PBE) study, however, finds very different adsorption geometries and energies.

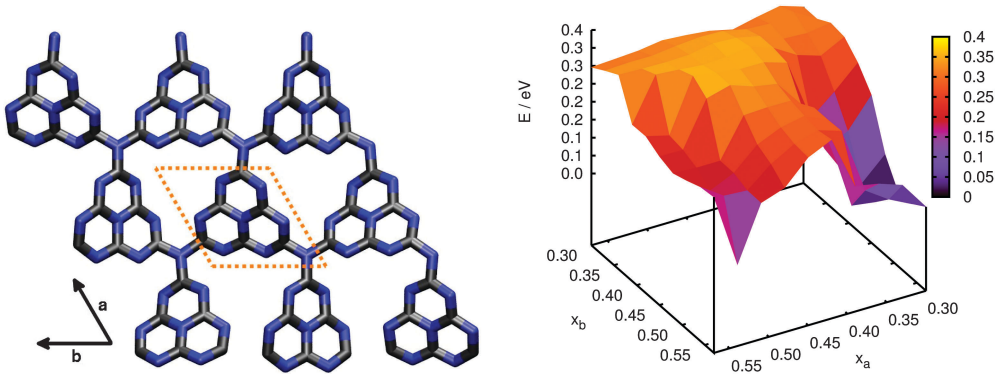

(a) Scan area (dotted orange frame) inside the reconstructed supercell.

(b) PES colormap plot for the selected area; the potential energy E is given relative to the global minimum.

Fig. 6 Relaxed PES scan of water adsorption in the (3 × 3) supercell model for an extended g-C_3N_4 sheet performed by periodic DFT calculations.

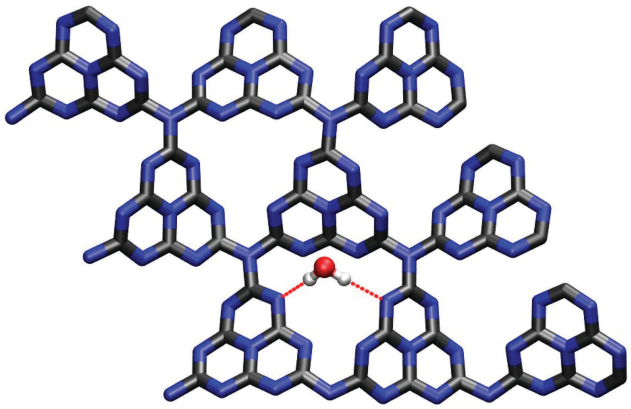

Fig. 7 Fully optimized water adsorption geometry in the global minimum configuration (PBE). Hydrogen bonds (2.02 and 2.19 Å, respectively) are indicated by dotted red lines, the interaction between water oxygen and the closest substrate carbon atom is purely electrostatic (distance: 2.84 Å).

Table 1 Maximum water adsorption energies for different surfaces studied in this work

	(0001) surface		($\bar{1}$010) surface
Method	PBE	DFTB	DFTB
E_{ads}/eV	−0.62	−0.34	−0.51

This might be, in part, due to it being based on a non-reconstructed (1 × 1) surface model, possibly not allowing for the favourable hydrogen bonded configuration in the substrate's pore. Therefore, direct comparison of our results to those of ref. 37 is not attempted here.

Apart from visualizing the preferred adsorption sites, Fig. 6(b) also allows for a semi-quantitative estimate of the diffusion barrier of water for transitions from one triangular substrate pore to a neighbouring one. Specifically, the saddle at $x_a = 0.42$ and $x_b = 0.57$ is about 0.3 eV higher in energy than the minimum configuration. Since most likely the actual barrier will be slightly lower considering the limited resolution of the PES scan, a barrier of 0.2 eV could be assumed as a lower limit guess yielding a diffusion rate of around 10^9 s^{-1} according to Eyring transition state theory.[38] This suggests a rather stable adsorption minimum on the timescale of molecular vibrations and charge transfer.

Subsequently, water adsorption was studied for the analogous (3 × 3) supercell in periodic SCC-DFTB calculations. For direct comparison, only a single g-C_3N_4 layer was considered in the first place, perfectly reproducing the previously found adsorption behaviour with the global minimum corresponding to the same hydrogen bonding situation in the triangular hole between two tri-*s*-triazine units. In contrast, regarding the absolute adsorption energy of $E_{ads} = -0.34$ eV as compared to −0.62 eV in the DFT calculation no perfect match can be observed (Table 1). This is, however, considering the method's semiempirical nature and its parametrization based on a different (hybrid) functional, not quite surprising and does not belittle the qualitative predictive power of these supporting calculations.

Therefore, in a next step the influence of additional g-C_3N_4 layers stacked along the [0001] direction in ABAB fashion on the water adsorption was studied by means of SCC-DFTB calculations. No difference in adsorption geometry or energy ($\Delta E_{ads} < 0.01$ eV) was observed for up to four substrate layers, confirming our original choice of a single-layer model (in the limitations of the applied methodology, see above) as sufficient for the description of g-C_3N_4-water interaction.

3.1.2 The ($\bar{1}$010) surface. Starting from the unit cell of a perfect ABAB crystal consisting of g-C_3N_4 layers stacked along the [0001] direction (*cf.* Fig. 4), four symmetrically equivalent surfaces of the ($\bar{1}$010) type can be created by vertical cuts along the cell's lattice vectors ***a*** and ***b*** as described in Section 2.3. This kind of hydrogen bearing surface is likely to feature different adsorption characteristics than its (0001) counterparts, although it is not quite clear how abundant it really is in experiment (or if it occurs at all), since individual g-C_3N_4 layers are mainly bound by dispersion forces and the barrier for lateral

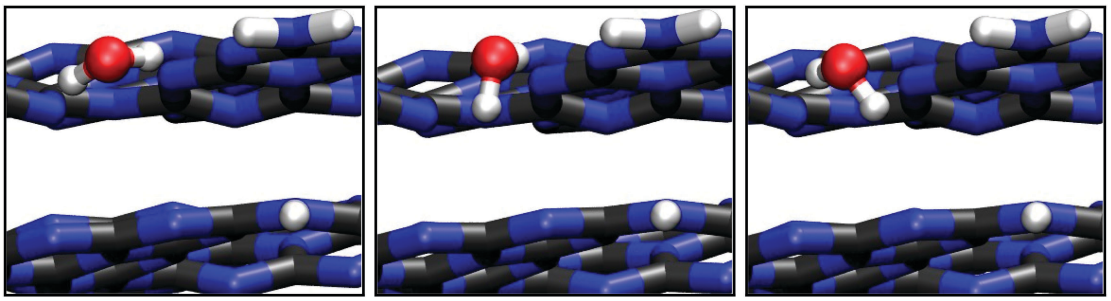

Fig. 8 Stable water adsorption geometries on the $(\bar{1}010)$ surface (SCC-DFTB) as mentioned in the text.

shearing might be rather small. Still, the hydrogen-rich situation present on this crystal cut can be regarded as a model also for defects stemming from incomplete condensation during synthesis which have been found to be relatively frequent.[2]

In contrast to the (0001) surface, the $(\bar{1}010)$ crystal cut offers three-dimensional adsorption pockets, stabilizing the water molecule not only by hydrogen bonds with the nitrogen lone pairs (bond length $\approx$ 2.0 to 2.5 Å) but also between the terminating amine groups and the water oxygen (distance $\approx$ 2.5 to 2.8 Å). Consistently, three different stable conformations were found in SCC-DFTB calculations, both varying in water orientation and adsorption energy (*cf.* Fig. 8). Interestingly, the latter, amounting to −0.43 eV (Fig. 8(c) and (b)) and −0.51 eV (Fig. 8(a)), only slightly exceeds the corresponding value for the (0001) surface and is clearly on the same order.

Overall, the stabilizing effect of residual hydrogen atoms terminating all but the (0001) surface does not seem to play a dominant role. Thus, the importance of these surfaces and/or similar defects for experimental observations will rather be governed by the question of their abundance, *i.e.* the question about the degree of polymerization of the sample which is highly preparation-dependent.[2] In the following, we can therefore restrict ourselves on the photocatalytic water decomposition on a well-defined (0001) surface, that is likely to be the dominant structure in highly ordered samples.

3.2 Photocatalytic water splitting

In the following, both half reactions of water decomposition according to eqn (1) and (2) are studied using a methodology described above. This approach, as outlined in Section 2.2, allows to estimate the respective overpotentials on the basis of a thermodynamic description of one-electron reaction steps and to identify the rate-limiting step. All calculations in this part are based on the periodic (3 × 3) single-layer model justified in the previous section, using DFT-PBE.

3.2.1 H_2O oxidation. To begin with the water oxidation reaction (producing molecular oxygen), in a first step, all adsorbate species occurring in eqn (4) to (7) (namely *O, *OH, and *OOH) were optimized by spin-polarized DFT calculations to include also effects due to the radical nature of the intermediates. As a starting point for each geometry optimization a position of the respective adsorbate above the hollow site, resembling the most favourable water adsorption configuration on the (0001) surface (*cf.* Fig. 7), was chosen, since performing a full PES scan for every intermediate would be computationally hardly feasible. This approach, however, seems justified by the fact that the intermediate species exhibit rather similar chemical characteristics to those of a water molecule and the most reactive substrate atoms are definitely the two-fold coordinated nitrogens with their lone pairs pointing into the triangular pores.

Furthermore, the resulting geometries (see Fig. 9) all come with rather high adsorption energies (Table 2), restraining potential diffusion processes and thus suggesting stable configurations on the timescale of electron transfer. Both the OH radical and OOH radical intermediate are stabilized mainly by electrostatic and hydrogen bonding interaction (E_{ads} = −0.61 and −0.66 eV, respectively), whereas the single oxygen intermediate is covalently bound to a substrate nitrogen, forming an N-oxide group which is also reflected in its exceptionally high adsorption/binding energy of −2.73 eV.

After optimization of the relevant gas phase molecules (namely H_2, O_2, and H_2O) using the same cell geometry and computational settings, normal mode analyses were performed for all species. These are used in eqn (8) to (11) for the corresponding free energy contributions. Assuming pH = 7, the resulting free energy steps during the reaction sequence are visualized in Fig. 10. Four different cases regarding the light-induced potential bias U are of special interest here:

(a) U = 0, describing the situation without any external potential, *i.e.* without irradiation of the sample. This energy profile is indicated by the continuous red line in Fig. 10, disclosing the first step (A, splitting of adsorbed water into adsorbed OH and formation of H^+ and e^-) with its pronounced endergonicity as rate-limiting for the whole process. The free energy difference required for step A is 2.28 eV under these conditions, which is a lower bound for the activation free energy. Note that in the Nørskov approach, activation energies are in fact not calculated and reaction energies serve as lower bounds for them. Obviously, the water dissociation reaction is hardly promoted by the g-C_3N_4 substrate which is in contrast to the situation previously found on metal oxide surfaces such as $TiO_2(110)$[27] or $RuO_2(110)$,[28] where the water molecule is covalently bound to surface metal atoms, weakening the intramolecular bonds.

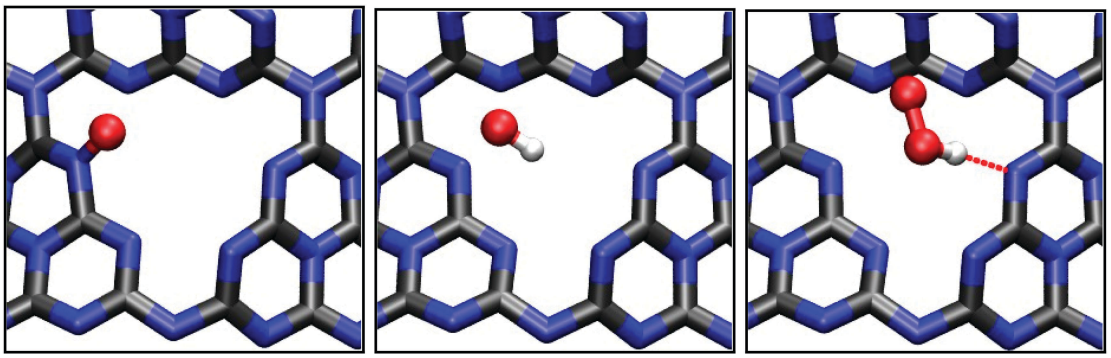

(a) O atom. (b) OH radical. (c) OOH radical.

Fig. 9 Optimized adsorption geometries (PBE) of intermediates during the water oxidation half reaction according to eqn (4) to (7). Selected bond lengths/atom distances: (a) r(N–O) = 1.28 Å; (b) r(N–O) = 2.28 Å, r(O–H) = 0.99 Å; (c) r(O–C) = 2.89 Å, r(O–O) = 1.34 Å.

Table 2 Adsorption energies (PBE, spin-polarized) of relevant species during photocatalytic water decomposition on the g-C_3N_4 (0001) surface according to the Nørskov model (*cf.* Section 2.2)

Species	H_2O molecule	O atom	OH radical	OOH radical	H atom	H_3O radical
E_{ads}/eV	−0.55	−2.73	−0.61	−0.66	−2.43	−3.39

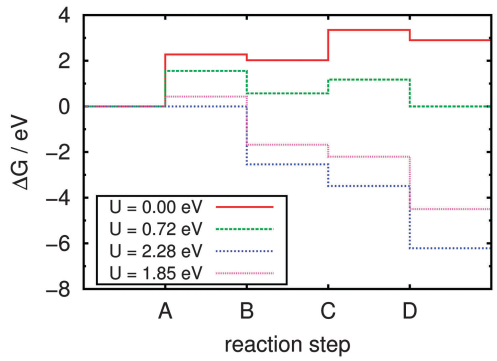

Fig. 10 Calculated free energy steps during the anodic water oxidation process at pH = 7. Continuous red line: no external potential/irradiation; dashed green line: equilibrium situation; dotted blue line: "all downhill" limit; dotted pink line: irradiated sample. No qualitative changes are observed for different values of pH; see text for a detailed discussion.

(b) The equilibrium situation (dashed green line in Fig. 10), marking the lower limit of bias U in which the overall reaction begins to be exergonic; this is the case above 0.72 V under the chosen conditions.

(c) The "all downhill" case (dotted blue line) starting from U = 2.28 V, in which all individual reaction steps are exergonic and the overall reaction will proceed spontaneously without kinetic hindrance (assuming the absence of individual barriers for the reaction steps).

(d) The case of the irradiated sample (dotted pink line) with all reaction steps shifted according to the potential of a photo-generated hole in the substrate valence band relative to the NHE; in ref. 8 this was estimated to be U_{VB} = 1.85 V at pH = 7 (see also Fig. 1).

Considering only the thermodynamic contribution to the overpotential, the latter is given by the difference between the potential biases in equilibrium and the "all downhill" case, yielding η_{ox} = (2.28 − 0.72) V = 1.56 V at 300 K and pH = 7. Temperature effects are generally small, because they influence the overpotential only *via* the enthalpic and entropic contributions to the free energies. There is no effect due to the pH term which is only imposing a constant shift on the energy scale; for the same reason there is no pH dependence of the overpotential in this model (as long as the pH term does not shift the overall reaction free energy to negative values).

In comparison, the free energy profile for the irradiated sample (dotted pink line in Fig. 10) still features one endergonic reaction step, which means that irradiation of the sample does not provide enough overpotential for the water oxidation half reaction to proceed spontaneously; according to this model an additional external bias of (2.28 − 1.85) V = 0.43 V would be needed to drive the whole sequence at pH = 7. According to ref. 8 the band positions relative to the NHE depend on the pH *via* $eU_{VB} \approx (2.20 - 0.05 \cdot \mathrm{pH})$ eV which is on the same order as the pH dependence of the redox potentials ($\Delta_{pH} = k_B T \ln(10) \cdot \mathrm{pH} \approx 0.06$ eV·pH). Therefore, the additional external potential needed for the reaction to take place despite irradiation of the sample only slightly changes from 0.50 V at pH = 0 to 0.36 V at pH = 14, *i.e.* the process cannot be driven by light at any pH. This finding is perfectly in line with the experimental observation that cocatalysts (such as Co_3O_4) are needed for water oxidation in any case,[4] lowering individual thermodynamic (and/or kinetic) barriers.

3.2.2 H^+ reduction. For comparison, also the second half-reaction, namely H^+ reduction, on the same substrate was studied using a similar approach as outlined in Section 2.2. Here, two different mechanisms were considered, either involving an additional water molecule adsorbed on the hollow site, or not (*cf.* eqn (14) and (15) or eqn (12) and (13), respectively).

Again, adsorption geometries of intermediate species (H atom, H_3O radical) were optimized on the hollow site (see Fig. 11), yielding large adsorption energies on the order of several eV (Table 2). This is easily understood by the strong covalent bond that is formed between a substrate N and adsorbate H atom, even

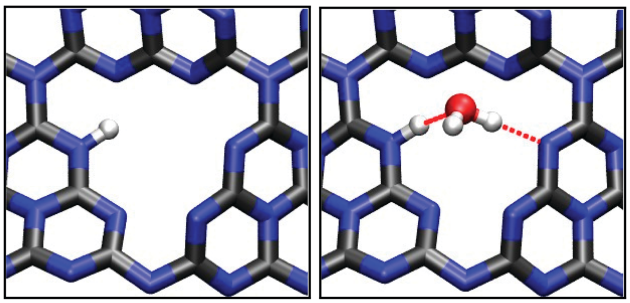

(a) H atom. (b) H_3O radical.

Fig. 11 Optimized adsorption geometries (PBE) of intermediates during the H^+ reduction half reaction according to eqn (12) and (14). Selected bond lengths/atom distances: (a) r(N–H) = 1.05 Å; (b) r(N–H) = 1.04 Å, r(O–C) = 2.81 Å, hydrogen bonds (dotted red lines) ≈ 2.85 Å.

subtracting one hydrogen atom in case of the H_3O radical, leaving the remaining water molecule in a hydrogen bonded configuration (Fig. 11(b)).

Evaluation of the free energy differences according to equations (16) to (19) at 300 K and pH = 0 or pH = 7 yields the values compiled in Table 3 for reaction steps E/E′ and F/F′, respectively. Here, in fact the pH plays a certain role, since the pH-related term easily overcompensates the slight endergonicity of step E/E′ in the two-step process. At pH = 0, cancelling the pH term in eqn (12) to (15), the U = 0 case is equal to the equilibrium situation and imposing a small bias of U = 0.03 V (U = 0.08 V, if including an additional water molecule), would cause the reaction sequence to proceed spontaneously, corresponding to a tiny overpotential of U = 0.03 V (U = 0.08 V). This overpotential is easily provided by a photo-generated electron in the conduction band whose corresponding potential relative to the NHE was estimated to be $U_{CB} \approx -0.50$ V at pH = 0 in ref. 8. At pH = 7, however, the pH term already causes the sequence to be "all downhill" even without the influence of any potential bias, *i.e.* the H^+ reduction half reaction is not subject to any overpotential under these conditions. The presence of an additional water molecule does not change the thermodynamics of the process significantly, as can be seen from the modest variations in Table 3.

The model applied here, however, does not consider possible effects due to additional potential barriers between the individual reaction steps as outlined above. Especially for the H^+ reduction half reaction featuring an extraordinarily large binding energy for the H intermediate which is most likely to hinder the following step, this approximation might not be sufficient for describing the kinetic origin of the overpotential. Here, also the effect of an additional water molecule in the proximity of the hydrogen atom will possibly play an important role in lowering the kinetic barrier for desorption. Still, the general finding that H^+ reduction on the g-C_3N_4 (0001) surface should be subject to a much smaller overpotential than H_2O oxidation is in very good agreement with the experimental observation that H_2 production is indeed possible under irradiation with visible light without any help of cocatalysts.[4]

Table 3 Free energy differences during photocatalytic H^+ reduction according to eqn (16) to (19) at 300 K

	pH = 0		pH = 7	
	Isolated H	Additional H_2O	Isolated H	Additional H_2O
$\Delta G_{E/E'}$	+0.03	+0.08	−0.38	−0.33
$\Delta G_{F/F'}$	−0.03	−0.08	−0.45	−0.50

4 Conclusions and outlook

In this combined first-principles and semiempirical study we systematically investigated water adsorption on graphitic carbon nitride, taking into account not only a perfectly crystalline sheet of the material but also the role of additional layers and surface terminations. The influence of layer stacking on the adsorption properties of the (0001) surface was found to be rather small, rendering a single-layer description of the system sufficient. Water adsorption was studied systematically for an infinite g-C_3N_4 sheet, revealing an optimal geometry with the water molecule bridging the triangular pore between three tri-*s*-triazine units by forming hydrogen bonds with substrate N atoms. The hydrogen-saturated ($\bar{1}$010) surface of a layered g-C_3N_4 ABAB crystal, possibly suitable as a model for defects in the material, was found to exhibit only slightly different adsorption qualities, mainly due to its amine functions.

Since, however, in a highly crystalline sample the (0001) surface should be by far most abundant, photocatalytic water splitting was studied on this surface afterwards. A method originally introduced by Nørskov and coworkers was used to model the water oxidation half reaction in a sequence consisting of four steps each of which providing an electron for H^+ reduction. Analysis of the individual reaction free energies revealed that, in contrast to similar investigations for metal oxide catalysts, the rate-limiting step in the oxidation process is in fact the water dissociation reaction on the substrate surface, possibly providing a starting point for the improvement of catalytic performance. A huge overpotential of 1.56 V was derived for this half reaction, preventing water oxidation from proceeding spontaneously upon irradiation of the sample irrespective of the solution's pH. This result is consistent with the experimental observation that O_2 evolution is in fact only possible in the presence of oxidation cocatalysts.

A similar formalism was set up for the H^+ reduction half reaction, consisting of two steps consuming an electron each. According to this model, hardly any overpotential (or none at all for larger values of pH) was found for H^+ reduction, rendering the photo-generated potential bias due to an electron in the substrate conduction band sufficient for driving the process at any condition of pH. This is, again, consistent with experiment, observing H_2 production under irradiation with visible light without help of cocatalysts.

Especially for the latter half reaction but also for water oxidation, further studies should concentrate on the "real" kinetic barriers of the individual reaction steps, adding to the overall overpotential. These could be found for example using a climbing-image

nudged-elastic band scheme.[39–41] Also, the influence of additional water molecules on the overpotential, *i.e.* its coverage-dependence, should be studied in some detail since experiments are generally conducted in aqueous solution. Apart from structural effects on the adsorption geometries of intermediates and their impact on the thermodynamics of the reaction sequence, especially the role of the water layer as a "source" or "sink" of protons is likely to influence both half reactions and the associated overpotentials. Another important step towards a direct interpretation of experimental observations would be to incorporate the role of cocatalysts in the model description of photocatalysis.

Concerning the goal of understanding charge separation, localization and exciton lifetime in graphitic carbon nitride as formulated in the introduction of this article, from the point of methodology a different approach than the one applied here has to be taken in order to calculate electronically excited states. On the basis of cluster models the whole toolbox of quantum chemistry is available, giving access also to excited states; additionally, the model for the description of water decomposition used in the present work could be reformulated in terms of charged intermediates in that case.[42] We already took first steps towards finding suitable g-C_3N_4 clusters, largely reproducing the water adsorption characteristics of our periodic model, and plan to improve on our description of photocatalytic water oxidation and H^+ reduction on graphitic carbon nitride in the near future.

References

1 X. Wang, S. Blechert and M. Antonietti, *ACS Catal.*, 2012, **2**, 1596–1606.
2 A. Thomas, A. Fischer, F. Goettmann, M. Antonietti, J.-O. Müller, R. Schlögl and J. M. Carlsson, *J. Mater. Chem.*, 2008, **18**, 4893–4908.
3 X. Wang, K. Maeda, A. Thomas, K. Takanabe, G. Xin, J. M. Carlsson, K. Domen and M. Antonietti, *Nat. Mater.*, 2009, **8**, 76–80.
4 K. Maeda, X. Wang, Y. Nishihara, D. Lu, M. Antonietti and K. Domen, *J. Phys. Chem. C*, 2009, **113**, 4940–4947.
5 F. Goettmann, A. Thomas and M. Antonietti, *Angew. Chem., Int. Ed.*, 2007, **46**, 2717–2720.
6 F. Su, S. C. Mathew, G. Lipner, X. Fu, M. Antonietti, S. Blechert and X. Wang, *J. Am. Chem. Soc.*, 2010, **132**, 16299–16301.
7 Y. Zhang, Z. Schnepp, J. Cao, S. Ouyang, Y. Li, J. Ye and S. Liu, *Sci. Rep.*, 2013, **3**, 2163.
8 Y. Zhang and M. Antonietti, *Chem. – Asian J.*, 2010, **5**, 1307–1311.
9 W. Kohn and L. J. Sham, *Phys. Rev.*, 1965, **140**, A1133–A1138.
10 P. E. Blöchl, *Phys. Rev. B: Condens. Matter Mater. Phys.*, 1994, **50**, 17953–17979.
11 G. Kresse and D. Joubert, *Phys. Rev. B: Condens. Matter Mater. Phys.*, 1999, **59**, 1758–1775.
12 G. Kresse and J. Hafner, *Phys. Rev. B: Condens. Matter Mater. Phys.*, 1993, **47**, 558–561.
13 G. Kresse and J. Hafner, *Phys. Rev. B: Condens. Matter Mater. Phys.*, 1993, **48**, 13115–13118.
14 G. Kresse and J. Hafner, *Phys. Rev. B: Condens. Matter Mater. Phys.*, 1994, **49**, 14251–14269.
15 J. P. Perdew, K. Burke and M. Ernzerhof, *Phys. Rev. Lett.*, 1996, **77**, 3865–3868.
16 J. P. Perdew, K. Burke and M. Ernzerhof, *Phys. Rev. Lett.*, 1997, **78**, 1396.
17 S. Grimme, J. Antony, S. Ehrlich and H. Krieg, *J. Chem. Phys.*, 2010, **132**, 154104.
18 S. Grimme, S. Ehrlich and L. Goerigk, *J. Comput. Chem.*, 2011, **32**, 1456–1465.
19 H. J. Monkhorst and J. D. Pack, *Phys. Rev. B: Solid State*, 1976, **13**, 5188–5192.
20 B. Aradi, B. Hourahine and T. Frauenheim, *J. Phys. Chem. A*, 2007, **111**, 5678–5684.
21 M. Elstner, D. Porezag, G. Jungnickel, J. Elsner, M. Haugk, T. Frauenheim, S. Suhai and G. Seifert, *Phys. Rev. B: Condens. Matter Mater. Phys.*, 1998, **58**, 7260–7268.
22 A. K. Rappe, C. J. Casewit, K. S. Colwell, W. A. Goddard and W. M. Skiff, *J. Am. Chem. Soc.*, 1992, **114**, 10024–10035.
23 L. Zhechkov, T. Heine, S. Patchkovskii, G. Seifert and H. A. Duarte, *J. Chem. Theory Comput.*, 2005, **1**, 841–847.
24 F. Jensen, *Introduction to Computational Chemistry*, Wiley, 2007.
25 J. K. Nørskov, J. Rossmeisl, A. Logadottir, L. Lindqvist, J. R. Kitchin, T. Bligaard and H. Jónsson, *J. Phys. Chem. B*, 2004, **108**, 17886–17892.
26 J. Rossmeisl, Z.-W. Qu, H. Zhu, G.-J. Kroes and J. Nørskov, *J. Electroanal. Chem.*, 2007, **607**, 83–89.
27 A. Valdés, Z.-W. Qu, G.-J. Kroes, J. Rossmeisl and J. K. Nørskov, *J. Phys. Chem. C*, 2008, **112**, 9872–9879.
28 J. Wirth, S. Monturet, T. Klamroth and P. Saalfrank, *EPL*, 2011, **93**, 68001.
29 E. Kroke, M. Schwarz, E. Horath-Bordon, P. Kroll, B. Noll and A. D. Norman, *New J. Chem.*, 2002, **26**, 508–512.
30 J. Gracia and P. Kroll, *J. Mater. Chem.*, 2009, **19**, 3013–3019.
31 M. Deifallah, P. F. McMillan and F. Cora, *J. Phys. Chem. C*, 2008, **112**, 5447–5453.
32 J. P. Perdew, *Int. J. Quantum Chem.*, 1985, **28**, 497–523.
33 W. Tang, E. Sanville and G. Henkelman, *J. Phys.: Condens. Matter*, 2009, **21**, 084204.
34 M. Dion, H. Rydberg, E. Schröder, D. C. Langreth and B. I. Lundqvist, *Phys. Rev. Lett.*, 2004, **92**, 246401.
35 J. Klimeøs, D. R. Bowler and A. Michaelides, *J. Phys.: Condens. Matter*, 2010, **22**, 022201.
36 J. c. v. Klimeš, D. R. Bowler and A. Michaelides, *Phys. Rev. B: Condens. Matter Mater. Phys.*, 2011, **83**, 195131.
37 S. M. Aspera, M. David and H. Kasai, *Jpn. J. Appl. Phys.*, 2010, **49**, 115703.
38 H. Eyring, *Chem. Rev.*, 1935, **17**, 65–77.
39 G. Mills, H. Jónsson and G. K. Schenter, *Surf. Sci.*, 1995, **324**, 305–337.
40 H. Jónsson, G. Mills and K. W. Jacobsen, *Classical and Quantum Dynamics in Condensed Phase Simulations*, World Scientific, 1995.
41 G. Henkelman, B. P. Uberuaga and H. Jónsson, *J. Chem. Phys.*, 2000, **113**, 9901–9904.
42 A. Valdés and G.-J. Kroes, *J. Phys. Chem. C*, 2010, **114**, 1701–1708.